Aeroelastic Response Simulation of a 3D Printed High Altitude Propeller

Malim, Ahmed; Mourousias, Nikolaos; Marinus, Benoît; De Troyer, Tim

Published in:
Proceedings of the AIAA AVIATION 2021 FORUM

DOI:
10.2514/6.2021-2490

Publication date:
2021

License:
Unspecified

Document Version:
Final published version

AIAA AVIATION Forum
August 2-6, 2021, VIRTUAL EVENT
AIAA AVIATION 2021 FORUM

10.2514/6.2021-2490

Aeroelastic Response Simulation of a 3D Printed High Altitude Propeller

Ahmed Malim*, Nikolaos Mourousias†
Royal Military Academy, Brussels, 1000, Belgium
Vrije Universiteit Brussel, Brussels, 1050, Belgium

Benoît G. Marinus‡
Royal Military Academy, Brussels, 1000, Belgium

Tim De Troyer§
Vrije Universiteit Brussel, Brussels, 1050, Belgium

This paper presents a steady aeroelastic simulation of a 3D Printed propeller blade designed for a High Altitude Platform Station (HAPS) by using the Fluid-Structure Interaction (FSI) method. On the fluid side, steady RANS simulations are carried out in ANSYS Fluent at an altitude of 16 km using the spring-based smoothing method to update the mesh. On the structure side, three materials are used to model the blade structure: two 3D-printed materials which are tough PLA and Onyx to print the blade core which is covered by a composite layer, and an aluminum blade as a benchmark. In order to model the 3D printed materials in ANSYS Mechanical, experimental tensile and bending tests have been performed first on dedicated samples according to the relevant standards. The experimentally fed material models are then used to perform tensile simulations on representative blade sections which are in turn compared to experimental tensile tests in order to validate the numerical approach. After several FSI-iterations, the aerodynamic performance of the rigid and the deformed blades are compared. It is found that the thrust and the torque generated by the deformed blades (FSI) are greater than those generated by the rigid blade (CFD only) for all materials. Also, the blade efficiency is impacted positively or negatively depending on the operating point.

Nomenclature

b	Blade section chord length	
C_f	Skin friction coefficient	$C_f = 2.\tau_w/(\rho.[V_\infty^2 + (2\pi nr)^2])$
C_P	Propeller power coefficient	$C_P = (2.\pi.Q)/(\rho.n^2.D^5)$
C_p	Pressure coefficient	$C_p = 2(p - p_\infty)/(\rho.[V_\infty^2 + (2\pi nr)^2])$
C_T	Propeller thrust coefficient	$C_T = T/(\rho.n^2.D^4)$
D	Diameter	
H	Altitude	
J	Advance ratio	$J = V_\infty/(n.D)$
n	Rotational velocity (rps)	
Q	Torque	
R	Propeller tip radius	
r	Radial position	
T	Thrust	
t	Blade section thickness	
V_∞	Flight velocity	

*PhD student in a joint framework between RMA and VUB, Department of Mechanical Engineering, avenue de la Renaissance 30. Email: ahmed.malim@vub.be
†PhD student in a joint framework between RMA and VUB, Department of Mechanical Engineering, avenue de la Renaissance 30
‡Professor, Department of Mechanical Engineering, avenue de la Renaissance 30, AIAA senior member.
§Professor, Department of Engineering Technology, Pleinlaan 5

β	Blade section twisting angle	
η	Propeller net propulsive efficiency	$\eta = J.C_T/C_P$
ρ	Density	
τ_w	Wall shear stress	

I. Introduction and Objectives

A. Introduction

In recent years, unmanned aerial vehicles (UAVs) and small-scale satellites have attracted the attention of researchers, military, and commercial companies and prompted them to think about exploiting their characteristics to integrate them into hybrid systems that are called High Altitude Pseudo-Satellites (HAPS). These stratospheric unmanned vehicles, used for telecommunications, internet services, environmental monitoring, and earth observation among others [1], can bring value in terms of performance and cost. In addition, they are maneuverable and easy to deploy, and they offer persistence and flexibility to complement satellites and drones. These systems also make flight cheaper, since for a given quantity of energy flying higher results in longer range, and can fly using solar power.

Efficient propulsion requires the use of a propeller as propulsive element in such applications. However, the low density and the low temperature of the air at high altitude make the propeller operate in a regime of high Mach and low Reynolds numbers accompanied by lower engine power absorption, stronger blade to blade interaction, and increased risk of flutter [2].

One of the most important aspects in the design of propellers is the structural aspect, which includes static, dynamic, modal, vibration, and fatigue evaluations. In addition, the coupling of the structural and aerodynamic aspects should be taken into account to perform an aeroelastic analysis early in the design phase. Such a multidisciplinary design is highly dependent on the material properties and the process by which the propeller blades are manufactured as well as the flight regime and the operating conditions.

Generally, the propellers are made out of wood, metal, or composite materials. Wood offers high strength-to-weight ratio, high fatigue strength, and great internal friction which makes it so effective at dampening vibrations. However, wood is prone to warping due to temperature and humidity, this warping can be minimized by constructing the propellers of several layers or laminations, all glued together. For higher performance, metal propellers were introduced. Steel and aluminum alloys have been extensively used and to a lesser extent magnesium and titanium alloys which offer also good properties from a structural standpoint. Due to their isotropic behaviour and their stiffness, metal propellers can be made, for high power and high rotational velocity, with very thin sections which are advantageous in terms of efficiency and to reduce centrifugal loads induced by the high material density coupled with high revolution speeds [3, 4]. Nowadays, composite materials are more commonly used. They are typically composed of high strength fibers, continuous or not, embedded in a low density matrix resin. Composite materials allow significant weight saving without altering the mechanical properties of the blade thanks to their excellent properties and resistance to fatigue [5]. However, the use of composite poses some issues regarding damage since they are more brittle than wrought metals, and regarding repair process which requires special conditions and equipment. Another manufacturing method, that is currently gaining popularity, is additive manufacturing (AM) or three-dimensional (3D) printing with metals or thermoplastics. In this work we focus on thermoplastics. It has been used to produce small scale propellers for Small Unmanned Aerial Vehicles (SUAV's) [6–9], and for large-scale 3D printing, it is slowly coming to the fore as a cost-effective solution for manufacturing large parts and components.

Additive Manufacturing techniques have become a widely used technology in recent decades for parts manufacturing and making products from a wide range of materials such as plastics, metal powder, ceramics and composites [10, 11]. This technology, due to its ease of use, economic accessibility, and variety of materials commercially available, was originally used to fabricate prototypes, hence the term rapid-prototyping. However, the current trend is to use AM in end-use components production and functional part manufacturing. AM enables to produce lightweight and durable parts, to design complex parts including complicated and internal features, to dispense with manufacturing tools, to save time and money included in tooling process, and to reduce material waste. These advantages allow it to gradually gain industrial sectors ranging from aerospace [12], biomechanics and biomedical engineering [13], transportation and automobile applications [14], architecture, building, and construction as well as electric and electronic devices [15]. Given the advantages of this technology, there is no doubt that it will have a promising future in the field of industry and production, and it will be able to revolutionize the future of propellers.

B. Objectives

The objective of this study is to perform a steady aeroelastic analysis of high altitude propeller blades, which are designed for High Altitude Pseudo Satellite (HAPS). Fluid-Structure Interaction (FSI) simulations are used to assess the stresses in the deformed blade under centrifugal and aerodynamic loads. The structural response of the propeller, under high altitude conditions (low density and low temperature), is analyzed in order to compare the aerodynamic performance for rigid (CFD) and deformed blade (FSI). The results are also compared with an aluminum blade as a benchmark.

The propeller structure is based on 3D-printed thermoplastic manufacturing for which the Finite Element Method (FEM) modeling of the 3D printed materials will be investigated through comparisons between experiments and FEM. The 3D-printed blade models are covered by an epoxy-glass fiber layer to improve the structural strength and obtain a smooth external surface.

FSI is the multiphysics study of how fluids and structures interact; the pressure loads applied by the fluid on the structure may cause structural deformations significant enough to change the fluid flow configuration itself. It can be performed using different fidelity levels. Low fidelity FSI models are typically based on the Blade Element Momentum (BEM) method and its extensions combined with different beam theories, whereas high fidelity models are based on the coupling between Computational Fluid Dynamics (CFD) and Computational Structural Dynamics (CSD) codes.

Aeroelastic analysis of a High Altitude composite Propeller (HAP) has been presented by Qu and Yang [16]. ANSYS Fluent and Mechanical APDL were used as CFD and CSD solvers respectively, and the composite propeller structure was modeled in Ansys ACP module. The same solvers were used by Carniea and Qin [17] to carry out a static linear aeroelastic analysis of a High Altitude Long Endurance (HALE) aircraft wing. Sodja et al [18, 19] conducted an FSI assessments of flexible Propeller Blades, that were modeled by using an isotropic material. They compared a low fidelity model, based on coupled extended blade-element momentum method and nonlinear beam theory, to high fidelity results obtained from the coupling of Ansys CFX and Ansys Mechanical.

II. Mathematical model

In this section, the general domain of FSI is defined, which consists of three parts: the fluid domain Ω_f and its boundaries Γ_f, the structure domain Ω_s and its boundaries Γ_s, and the fluid-structure interface Γ_i as shown in Fig .1. After that, the governing equations that need to be solved for both domains are presented. Finally, the equilibrium and compatibility conditions that must be satisfied at the fluid-structure interface are defined.

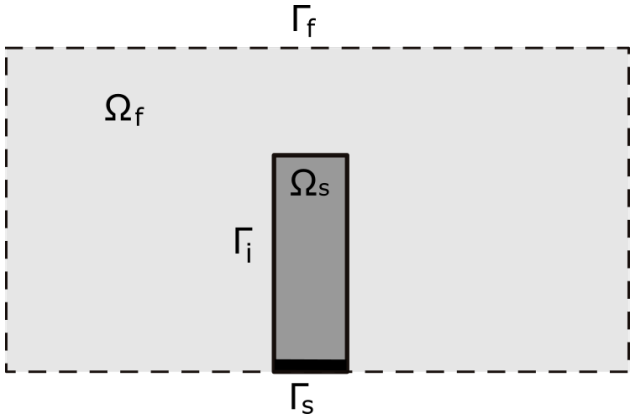

Fig. 1 General domain of FSI.

A. Navier-Stokes equations in rotating reference frame

The Navier-Stokes equations in an inertial (non-accelerating) reference frame are given below:

$$\frac{\partial \rho}{\partial t} + \nabla.(\rho \vec{v}) = 0 \tag{1}$$

$$\frac{\partial(\rho\vec{v})}{\partial t} + \nabla.(\rho\vec{v}\vec{v}) = -\nabla p + \nabla.(\overline{\overline{\tau}}) + \rho\vec{g} + \vec{F} \tag{2}$$

where $\vec{v}$ is the absolute velocity (the velocity viewed from the inertial frame), p is the static pressure, $\overline{\overline{\tau}}$ is the fluid stress tensor, and $\rho\vec{g}$ and $\vec{F}$ are the gravitational body force and external body forces respectively.

For a rotating flow (without translation), the equations can be written relatively to a rotating reference frame, with a rotational velocity $\vec{\omega}$, by defining the relative velocity $\vec{v_r}$ (the velocity viewed from the rotating frame) and the entrainment velocity $\vec{u_r}$:

$$\vec{v_r} = \vec{v} - \vec{u_r} \tag{3}$$

and

$$\vec{u_r} = \vec{\omega} \times \vec{r} \tag{4}$$

By injecting the Eq. (3) and Eq. (4) in the flow equations Eq. (1) and Eq. (2), and by considering a constant rotational velocity ($\frac{d\vec{\omega}}{dt} = 0$), the flow equations can be written in the relative system as follows:

$$\frac{\partial\rho}{\partial t} + \nabla.(\rho\vec{v_r}) = 0 \tag{5}$$

$$\frac{\partial(\rho\vec{v_r})}{\partial t} + \nabla.(\rho\vec{v_r}\vec{v_r}) + \rho(2\vec{\omega} \times \vec{v_r} + \vec{\omega} \times \vec{\omega} \times \vec{r}) = -\nabla p + \nabla.(\overline{\overline{\tau_r}}) + \rho\vec{g} + \vec{F} \tag{6}$$

For a steady flow ($\frac{\partial}{\partial t} = 0$), the Eq. (5) and Eq. (6) become:

$$\nabla.(\rho\vec{v_r}) = 0 \tag{7}$$

$$\nabla.(\rho\vec{v_r}\vec{v_r}) + \rho(2\vec{\omega} \times \vec{v_r} + \vec{\omega} \times \vec{\omega} \times \vec{r}) = -\nabla p + \nabla.(\overline{\overline{\tau_r}}) + \rho\vec{g} + \vec{F} \tag{8}$$

where $\vec{r}$ is the position vector from the origin of the rotating frame.

B. Structural equation

The Lagrangian equation of the motion of a structure is:

$$\rho_s \frac{\partial^2\vec{u}}{\partial t^2} = \nabla.(\overline{\overline{\tau_s}}) + \vec{f^B} \tag{9}$$

where ρ_s is the solid density, $\vec{u}$ is the structural displacement vector, $\overline{\overline{\tau_s}}$ is the Cauchy stress tensor, and $\vec{f^B}$ is the body forces vector.

with as boundary conditions:

$$\begin{aligned} \vec{u} &= \vec{u_S} \text{ on } S_u \\ \overline{\overline{\tau_s}}.\vec{n} &= \vec{f^S} \text{ on } S_f \end{aligned} \tag{10}$$

where S_u and S_f represent the parts of the boundary with prescribed displacement $\vec{u_S}$, and traction $\vec{f^S}$ respectively, and $\vec{n}$ is a unit outward normal vector to the boundary.

The Finite Element Method (FEM) is used to analyze the rotating blade. The discretized equations of a structure (without dissipation) can be written as follow:

$$M\ddot{u} + Ku = F_G + F_C + F_A \tag{11}$$

where M is the mass matrix, K is the stiffness matrix, u is the nodal displacement, the double dots represent the second derivative with respect to time, F_G is the constant gravity load matrix, F_C is the equivalent centrifugal force matrix resulting from the propeller rotational speed, and F_A is the aerodynamic force which is updated at each coupling step during the FSI simulation.

As the steady assumption (static structural analysis) is considered in this study, the structural equations are written as bellow:

$$Ku = F_G + F_C + F_A \tag{12}$$

C. Fluid structure interaction

When a viscous fluid flow is interacting with a structure, equilibrium and compatibility conditions must be satisfied at the fluid-structure interface Γ_i as the following equations describe:

$$\begin{aligned} \vec{u_f} &= \vec{u} \\ \vec{v_r} &= \frac{d\vec{u}}{dt} \\ \overline{\overline{\tau_r}}.\vec{n_f} &= -\overline{\overline{\tau_s}}.\vec{n_s} \end{aligned} \tag{13}$$

where $\vec{n_f}$ and $\vec{n_s}$ are the unit normal vectors that point outward from the domains Ω_f and Ω_s respectively, and u_f is the fluid domain displacement.

A steady coupled analysis is used for the fluid-structure interaction calculation using ANSYS System Coupling in Workbench (co-simulation). An iteration-based method is selected which has multiple coupling iterations and one coupling step. As opposed to the step-based method (multiple coupling steps), which stores restart data at the end of each coupling step and offers the possibility to restart the simulation from the previous step in case of interruption at the expense of file storage space, the iteration-based method generates results and restart data only at the end of the simulation (the end of the unique coupling step) leading to file storage space minimization at the expense of the ability to restart the analysis. System Coupling manages the data transfers (force and displacement) between the coupling participants (Fluent and Mechanical solvers) via the mapping process, which allows the use of the data from locations on a source mesh to calculate data for locations on a target mesh, using as convergence criterion the Root Mean Square (RMS) of the change in the transferred force and displacement. To ensure 100% of nodes are mapped and the transferred force is conserved, the finite element mesh should be fine enough and the reaction force in the structural model should be similar to the force obtained by CFD. For this purpose, one-way FSI simulations have been performed by applying the flow field pressure on the blade surface using different finite element meshes until getting stresses and displacements independent of the mesh as well as the transferred force conservation and the totality of the nodes mapped. The results of these one-way FSI will be discussed in Section IV.A.

After each coupling iteration, the fluid solver needs to update the mesh. The spring-based smoothing method is used for this purpose. A spring is assumed to connect between any two mesh nodes and if a given node undergoes a displacement, a force proportional to the displacement will be generated along all the springs connected to the node. By Hooke's law, the force on the node can be written as:

$$\vec{F_i} = \sum_{j}^{n_i} k_{ij}(\Delta\vec{x_j} - \Delta\vec{x_i}) \tag{14}$$

where n_i is the number of neighboring nodes connected to node i, $\Delta\vec{x_i}$ and $\Delta\vec{x_j}$ are the displacements of node i and its neighbor j, and k_{ij} is the spring stiffness defined as:

$$k_{ij} = \frac{k_f}{\sqrt{|\vec{x_i} - \vec{x_j}|}} \tag{15}$$

where k_f is the the spring constant factor defined in Fluent dynamic mesh parameters. At equilibrium, the net force must be zero which gives the following iterative equation, that is solved during the dynamic mesh update by using user defined iteration number m and convergence tolerance:

$$\Delta\vec{x}_i^{m+1} = \frac{\sum_{j}^{n_i} k_{ij}\Delta\vec{x}_j^{m}}{\sum_{j}^{n_i} k_{ij}} \tag{16}$$

After the convergence of the iterative process, the converged solution $\Delta\vec{x}_i^{converged}$ will be added to the old node position to obtain its new position as bellow:

$$\vec{x}_i^{n+1} = \vec{x}_i^{n} + \Delta\vec{x}_i^{converged} \tag{17}$$

III. Numerical model verification

A. CFD model validation

The propeller blade geometry is obtained from the exploratory optimization process that has been performed in [2]. The most efficient candidate has been chosen for this study, which is a four-bladed (04) propeller obtained from optimization round E with Clark-Y airfoils and diameter D = 1.9 m. Due to the lack of experimental data at high altitude, The NACA 4-(5)(05)-041 four bladed single rotation propeller [20] with diameter of D = 1.22 m, for which experimental data is available, is used to validate the CFD model using ANSYS Fluent 2021 R1 with implicit density based solver and the $k-\omega$ SST turbulence model. For the 3D CFD domain, a quarter cylinder is considered in order to model a single blade passage to exploit the periodicity and reduce the simulation time. The boundary conditions are shown in Fig .2 and Table .1 and the domain dimensions are 1 D between the inlet and the blade location, 3 D between the outlet and the blade location, and the quarter cylinder radius is 2.5 D.

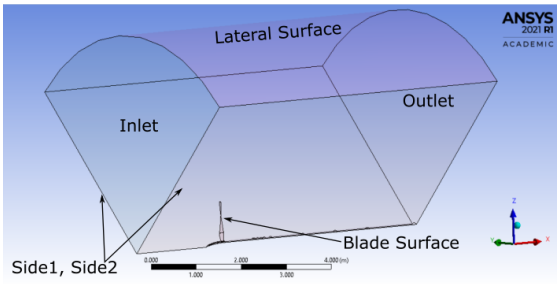

Fig. 2 Fluid domain.

Name	Type	Value
Inlet	Velocity inlet	$(V_\infty, 0, 0)$
Lateral Surface	Velocity inlet	$(V_\infty, 0, 0)$
Outlet	Pressure outlet	$p_{Gauge} = 0Pa$
Side 1, Side 2	Periodic	Angle = 90°
Blade Surface	Wall	No slip
Spinner Surface	Wall	No slip

Table 1 Boundary conditions.

A mesh study has been performed for the NACA propeller using six (06) unstructured tetrahedral meshes and six (06) operating points as shown in Fig .3a where the mesh of 3.56 10^6 elements is considered accurate enough, yet numerically light enough given the demanding resources for FSI, to give converged and independent propulsive efficiency. The NACA propeller propulsive efficiency obtained from the considered mesh is compared to the experimental results as shown in Fig .3b with an error of 2% for Mach = 0.1 and 3% for Mach = 0.2 over several advance ratios.

The same model and the same mesh strategy is used to perform the CFD analysis of the optimized four-bladed (04) high altitude propeller 'E' using six (06) unstructured tetrahedral meshes and five (05) operating points under 16 km altitude conditions. The air properties are obtained from the standard atmosphere and the flight velocity is supposed to be constant V_∞ = 77.6 $m.s^{-1}$. The blade shape and geometrical radial distributions are shown in Fig .4.

The 4.76 10^6 elements mesh is chosen to be used in the further study as shown in Fig .5a. This mesh is built with the same methodology as the 3.56 10^6 mesh of the NACA propeller but differs in the tip diameter. It features 24 inflation layers in the first 4mm normal to the wall and has a non-dimensional normal distance y+ between 0.03 and 2 with an average value of 0.6. Fig .5b shows the propulsive efficiency map at 0 and 16 km of altitude. The sea level performance has been calculated to estimate the generated thrust during the take-off that must be high enough to overcome the aircraft total drag and greater than a given value. Table (2) gives the thrust values at 0 and 16 km at different operating points. The results also show that the propeller can ensure an efficient take-off by generating a propulsive power of 126 kW and 236 kW for the most two (02) efficient operating points (J= 1.4 and J= 1.25) respectively with an efficiency greater than 80%.

B. Solid model validation

The main structure of each single blade consists of a thermoplastic 3D printed core and an epoxy-glass fiber skin. The Fused Deposition Modeling (FDM) technique is used to 3D print two (02) thermoplastic materials which are Onyx

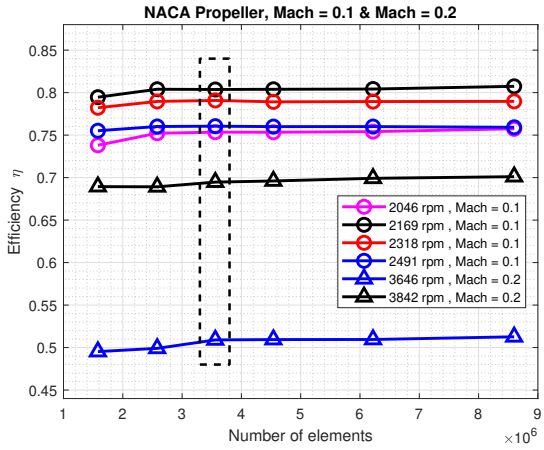

(a) Efficiency vs number of elements.

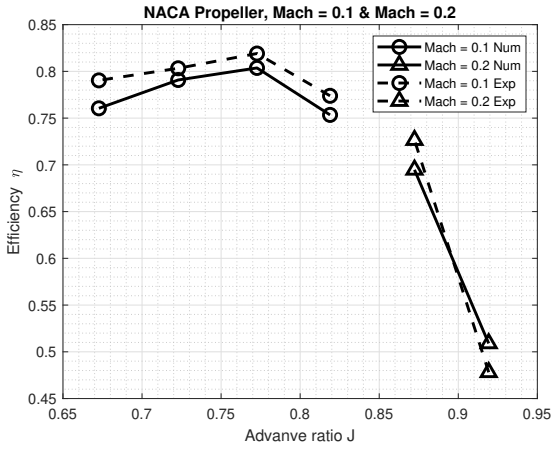

(b) Efficiency vs advance ratio.

Fig. 3 NACA4-(5)(05)-041 propeller mesh study.

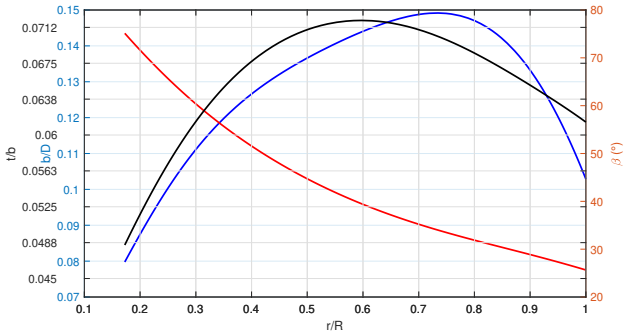

(a) Chord, thickness, and twisting angle radial distributions.

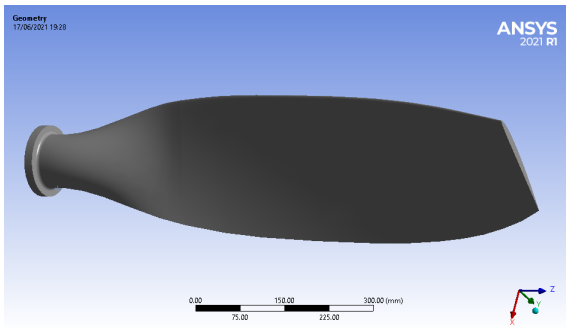

(b) Blade geometry with shank.

Fig. 4 Optimized four-bladed (04) high altitude propeller blade (propeller 'E' from Ref[2]).

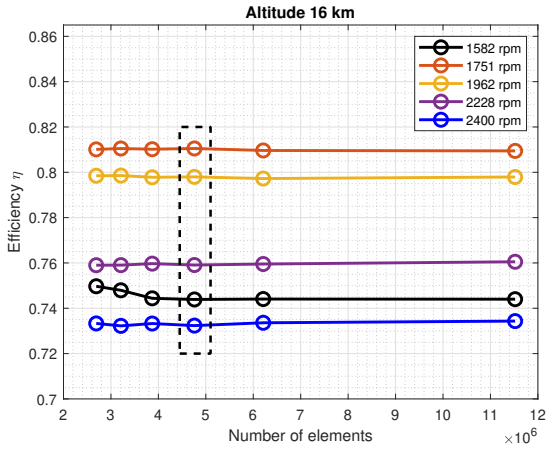

(a) Efficiency vs number of elements.

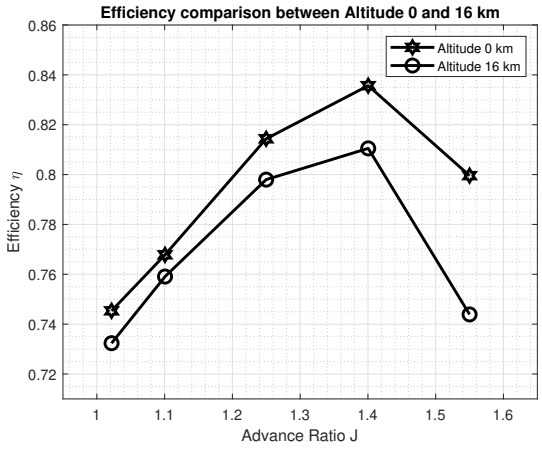

(b) Efficiency vs advance ratio.

Fig. 5 Optimized four-bladed (04) high altitude propeller mesh study (propeller 'E' from Ref[2]).

Table 2 Thrust T and torque Q at 0 and 16 km altitude.

H (km)	rpm	T (N)	Q (N.m)	$T_{tot}(N)$	$Q_{tot}(N.m)$
0	1582	162.0	94.9	648	379.6
	1751	405.8	205.6	1623.2	822.4
	1962	762.2	353.8	3048.8	1415.2
	2228	1288.4	558.5	5153.6	2234
	2400	1679.2	696.1	6716.8	2784.4
16	1582	20.5	12.9	82	51.6
	1751	53.3	27.8	213.2	111.2
	1962	101.1	47.9	404.4	191.6
	2228	171.7	75.2	686.8	300.8
	2400	223.9	94.5	895.6	378

and Tough PLA printed by Markforged and Ultimaker S5 printers respectively. The validation process of the numerical models of the 3D printed materials is shown in the flowchart of Fig .6

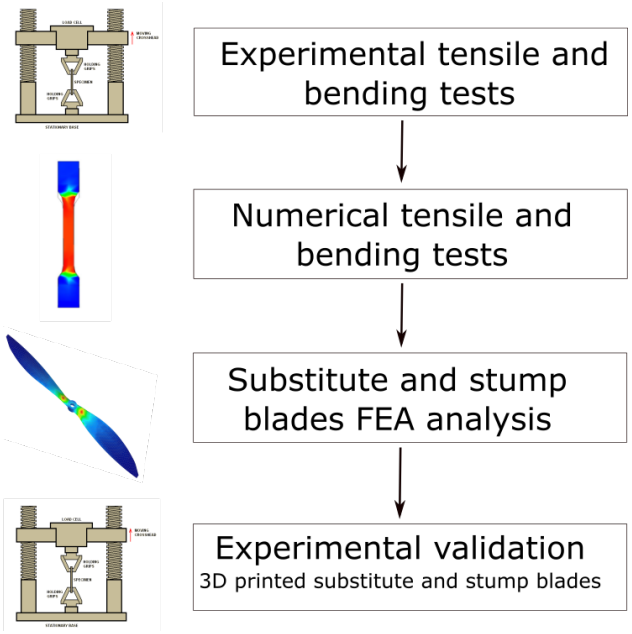

Fig. 6 3D printed material model validation strategy.

- **Experimental tensile and bending tests**
  Different test samples have been printed in Onyx and Tough PLA prior to testing using a Zwick-Roell BZ1-MM100M1.UT07 universal testing machine. Table .3 shows the 3D printing together with the tests parameters.

Table 3 Tensile and 3-point bending samples printing and testing parameters.

Test	Standard	N° of samples	Layer thickness (mm)	Direction	Orientation	Test speed (mm/min)
Tensile	ISO 527-2/1A	5	0.1 and 0.2	0/90°, –45/45°	Flat, vertical	5
Bending	ASTM D5023	5	0.1 and 0.2	0/90°, –45/45°	Flat, vertical	2

The tensile tests showed that the two (02) materials Onyx and Tough PLA have different behaviour: tough PLA behaves like a brittle material where the majority of the stress-strain curve is linear, whereas Onyx has a nonlinear

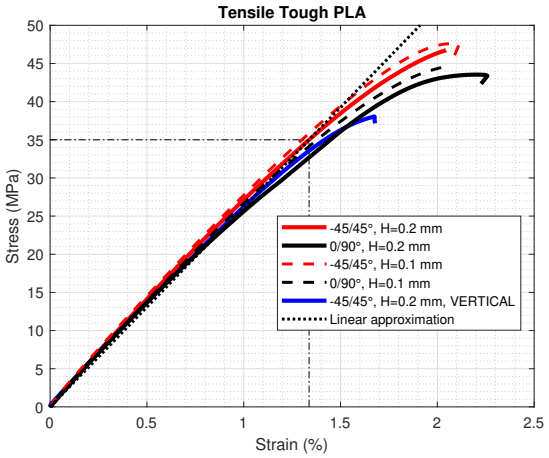

(a) Tough PLA.

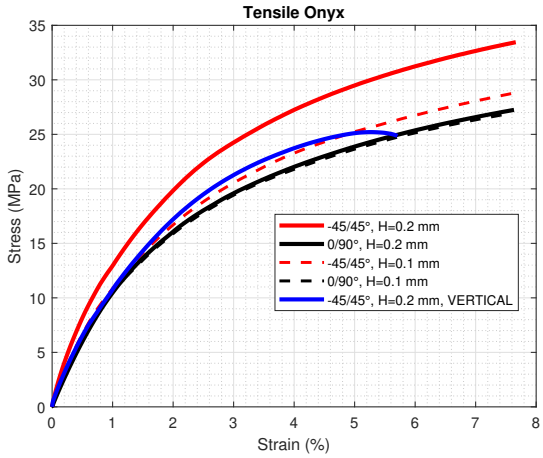

(b) Onyx.

Fig. 7 Stress-strain tensile curves.

behaviour without yield point [21]. The results also showed that both materials have the same behaviour when they are printed in the flat (XY plane) and vertical (Z) orientation, with almost the same strength but 20% and 26% lower breaking point in the vertical orientation for tough PLA and Onyx respectively. The samples printed in $(-45/45°)$ filament direction showed better results in terms of strength and breaking point, while the layer thickness has a negligible influence on the printed part strength but the printing time is doubled when using layer thickness 0.1 mm instead of 0.2 mm.

The stress-strain tensile curves, for different printing parameters, are shown in Fig .7. Each curve is obtained by averaging the five (05) experimental curves.

Combining this data, the two materials could be approximated to isotropic materials or transversely isotropic (isotropic in the XY plane with lower breaking point in the Z orientation). In this study, the isotropic assumption is considered with printing layer thickness 0.2 mm to save the half of the printing time, and filament printing direction $-45/45°$ for being stronger than $0/90°$ in all cases.

- **Numerical tensile and bending tests**

  For Tough PLA, the linear elastic isotropic model is used by introducing the experimental Young modulus (E= 2617 MPa) and considering the end of the linear part of the curve as the maximum tolerable stress that could be applied on the printed part as shown in Fig .7a. After that, a numerical three-point bending test is performed using ANSYS Mechanical 2021 R1. Next, we compare the numerical and the experimental Force-Displacement curves as shown in Fig .8a. The bending numerical results match precisely the experimental ones in the linear region. In other words, the use of the linear isotropic model, obtained from tensile test, for the 3D printed tough PLA gives accurate numerical results for another solicitation (bending), which is the second most important load case for the propeller blade FSI since the blade undergoes bending due to the generated thrust and torque.

  For Onyx, the hyper-elastic experimental data toolbox in ANSYS is used to model the nonlinear behaviour. This tool allows the import of experimental stress-strain curves by using the Response Function feature (RF) to create a new material and use it in different analyses. Fig .8b and Fig .8c show the numerical and experimental tensile and bending tests of Onyx material. A good agreement can be seen for low forces, and the difference increases by moving to high forces.

- **Blade section test**

  The objective of this step is to apply the material models on other 3D printed shapes, and compare the numerical and experimental results for validation. Two (02) substitute blades have been printed with Onyx and Tough PLA and one (01) stump blade is printed by Tough PLA (total length is 34 cm which is the maximum allowable length in Ultimaker S5). The 3D printed blades CAD are shown in Fig .9. The printed blades are then tested in tension (tensile) using a designated test bench that is machined to be mounted in the Zwick Roell testing machine and transmit tensile loads fairly to substitute blades or stump blades such as in Fig .9a and Fig .9b respectively. One side is fixed by pins (for the substitute blade) and by a fixed hub (for the stump blade) and the other side is pulled

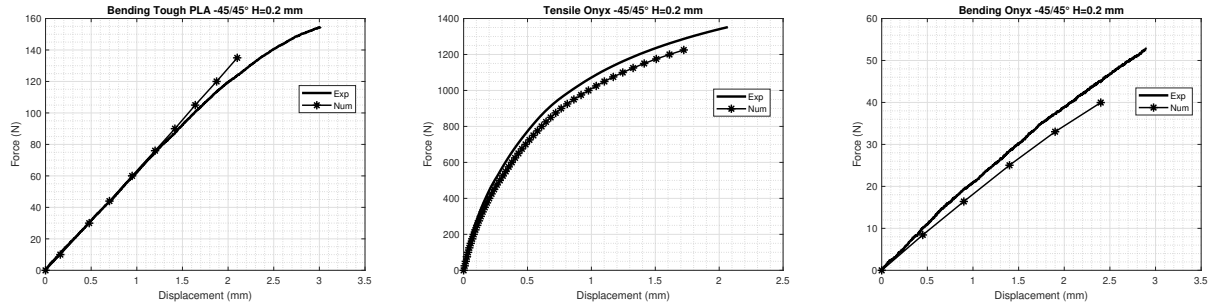

(a) Bending Tough PLA. (b) Tensile Onyx. (c) Bending Onyx.

Fig. 8 Experimental and numerical Force-Displacement curves for samples.

using pins through a piece that is fixed on the moving part of the machine.

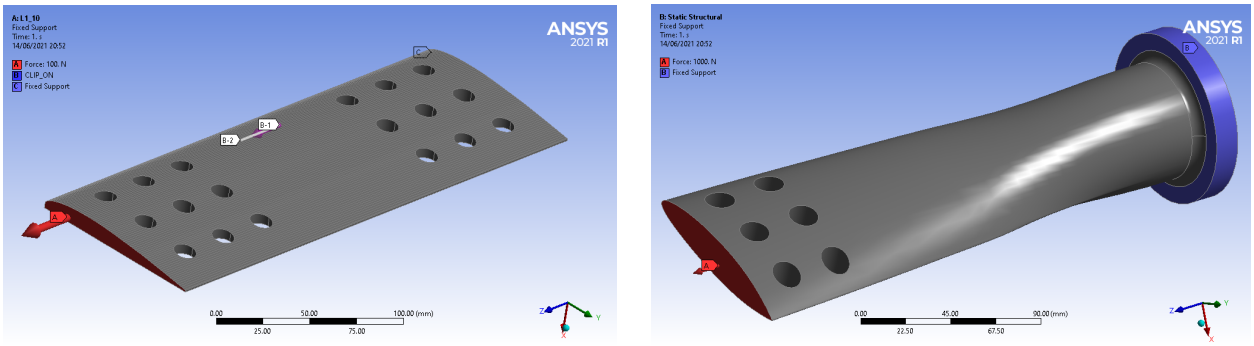

(a) Substitute blade. (b) Stump blade.

Fig. 9 3D printed test blades CAD.

Fig .10 shows the experimental and numerical force-displacement curves of the 3D printed blades. Two (02) displacement measurements have been done for the tough PLA and the Onyx substitute blades, a total blade displacement using the machine crossbar and a local displacement, measured in the middle of the blade close to the leading edge side, using extensometer (clip-on with L_0 = 30 mm) as shown in Fig .9a. From Fig .10a, It can be seen that the numerical results have good agreement with the experimental results for the tough PLA substitute blade, within 4% and 6% of difference in global and local displacements respectively (measured at maximum applied force 7 kN). The Onyx substitute blade shows good agreement for low forces, but remarkable differences appear for high forces as shown in Fig .10b, within 20% of difference for both global and local displacements (measured at maximum applied force 4 kN). For the stump blade on tough PLA, Fig .10c shows the global displacement measurement. the graphs show good agreement between the numerical and experimental results within 8% of difference (measured at maximum applied force 25 kN).

Since the 3D printed cores are covered by a composite layer that is supposed to support the majority of the loads, they undergo relatively low stress levels, insuring acceptable limits to operate away from failure. The validated 3D printed material models will be used in FSI.

IV. Results

For the results, two (02) operating points are considered for the FSI, which are the most two (02) efficient operating points (J= 1.4 and J= 1.25) with rotational velocity 1751 rpm and 1962 rpm respectively. As the material density value is crucial in the centrifugal force, the 3D printed materials densities are calculated by the division of the 3D printed samples mass by their volume. So we get for Onyx $\rho_{Onyx} = 1052\ kg/m^3$ and for Tough PLA $\rho_{TPLA} = 1100\ kg/m^3$. The aluminum alloy defined in ANSYS engineering data is used for the benchmark ($\rho = 2770\ kg/m^3$, $E = 71GPa$,

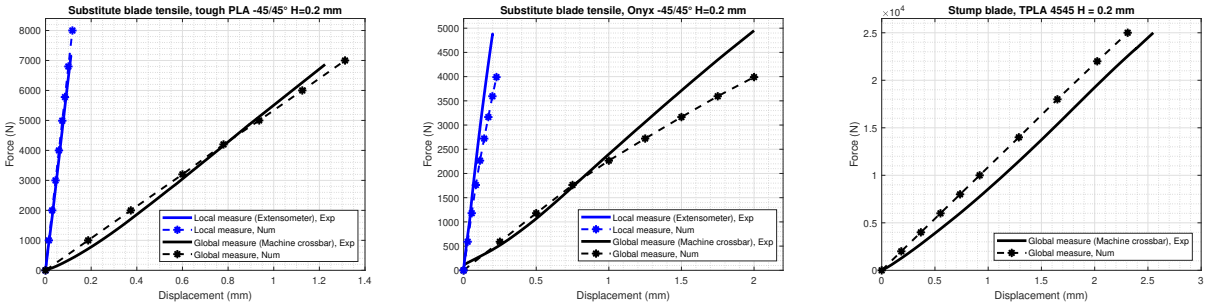

(a) Substitute blade on tough PLA. (b) Substitute blade on Onyx. (c) Stump blade on tough PLA.

Fig. 10 Experimental and numerical Force-Displacement tensile curves of the substitute and the stump blades.

$\nu = 0.33$). The composite layer consists of Epoxy S-Glass UD ($\rho = 2000\ kg/m^3$, $E_X = 50$ GPa, $E_Y = 8$ GPa, $E_Z = 8$ GPa, $\nu_{XY} = 0.3$, $\nu_{YZ} = 0.4$, $\nu_{XZ} = 0.3$).

A. One way FSI

For the one way FSI mesh study, four (04) finite element meshes have been used for each blade structure. The Von Mises stress, the total deformation, and the reaction force at the blade root are checked to assess the mesh convergence. All the meshes achieved 100% of mapped nodes during the import of the pressure field from the CFD results. For a given element size, the mesh of the aluminum blade always contains less elements than the two other structures due to the dedicated mesh for the epoxy-glass fiber layer. In this case, the mesh convergence needs more refinement due to the complexity of the model as shown in Fig .11

In Fig .11a, the stresses in the 3D printed cores are multiplied by 10 to show them in the same graph. It can be seen that the majority of the stresses are supported by the composite layer which can largely resist them, and the stresses in the cores are within acceptable limits. For the reaction force at the blade root, it can be seen, in Fig .11c, that the opposite value of the thrust is equal to the reaction force for the third and the fourth meshes, so the transferred force from the CFD is conserved within 99%. In further study, the third finite element mesh (1.77 10^5 elements) is used for the 3D printed blades simulations and the second finite element mesh (1.04 10^5 elements) is used for the aluminum blade.

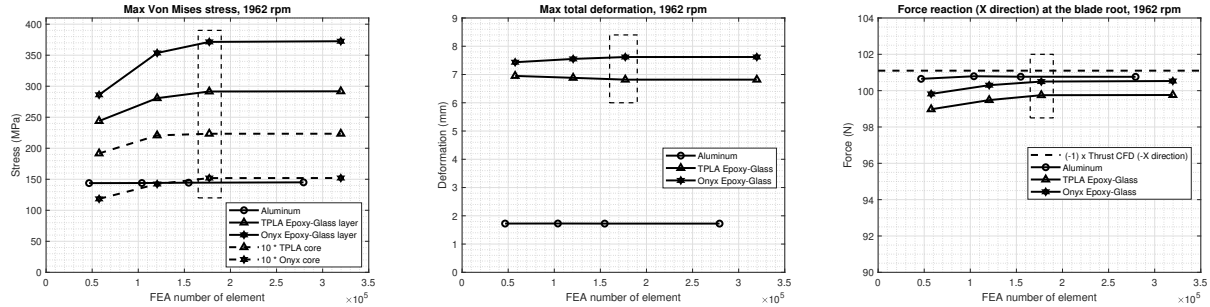

(a) Max Von Mises stress. (b) Blade total deformation. (c) Force reaction at the blade root.

Fig. 11 Finite element mesh study.

B. Steady two way FSI

Stresses and deformations

Before discussing this item, it is better to remind that the flight direction is $+X$ so the thrust direction is $-X$, and the blade rotation is around the X axis ($\vec{\omega} = +\omega\vec{X}$) so the torque direction is $\vec{Q} = -Q\vec{X}$.

The 3D printed tough PLA blade model is chosen to study the stresses and the deformations at 1962 rpm which generates highest loads. The case of a blade under centrifugal force only is compared with the case of a blade assessed by FSI (centrifugal and aerodynamic forces). Since the aerodynamic forces depend strongly on the altitude, the FSI case is analyzed at 0 km and 16 km. Fig .12 and Fig .13 show the tip view of the blade X-deformation and Y-deformation for the three (03) cases. The original (non deformed) blade is shown in wire-frame using the true scale for all the cases.

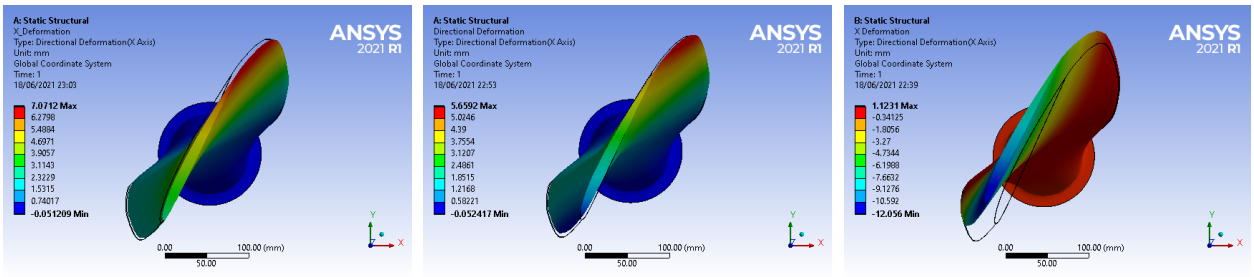

(a) Centrifugal force only. (b) FSI at H=16 km. (c) FSI at H=0 km.

Fig. 12 3D printed tough PLA blade X-deformation at 1962 rpm.

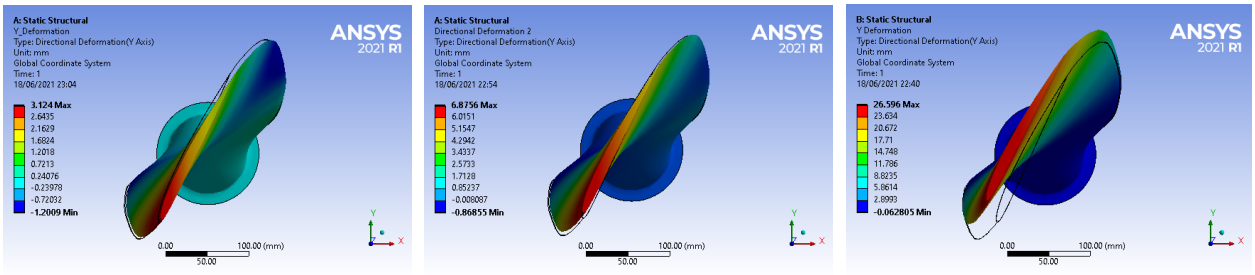

(a) Centrifugal force only. (b) FSI at H=16 km. (c) FSI at H=0 km.

Fig. 13 3D printed tough PLA blade Y-deformation at 1962 rpm.

It can be seen that, under centrifugal force only (Fig .12a and Fig .13a), the X-deformation is positive in all the blade with a maximum value of 7.07 mm in the trailing edge of the tip region, whereas the Y-deformation is positive in the leading edge and negative in the trailing edge, resulting in an increase of the airfoils angle of attack (centrifugal twisting moment). At altitude of 16 km, the generated thrust tends to reduce the centrifugal X-deformation towards negative values, while the torque force continues increasing the Y-deformation as shown in Fig .12b and Fig .13b. Since the center of pressure is located in the first half of the chord length as shown in the pressure coefficient graphs, the thrust tends also to twist the blade towards higher angle of attack, which explains the gain of 15.2% in thrust. In this case, the centrifugal force is dominant in terms of deformation due to the relatively low values of the aerodynamic forces generated at high altitude. At sea level H= 0 km, the thrust is seven (07) times higher (Table .2). Fig .12c and Fig .13c show that the aerodynamic forces are dominant in terms of deformation.

For the stress analysis, the equivalent (Von Mises VM) stress and the normal stress (normal to Z axis) are used as criteria to evaluate the 3D printed core and the composite layer respectively. Since the stresses are analyzed by evaluating their maximum values, the blade FSI at H= 0 km, for which the aerodynamic forces are more important, is chosen to compare with the blade under centrifugal force only as shown in Fig .14. It can be seen that the composite layer, for which the stress limit is 1700 MPa, can largely resist the generated stresses, and for the 3D printed core stresses are within acceptable limits for both cases.

Performance comparison

The comparison between the rigid (CFD) and the deformed (FSI) blade performance is done by calculating the thrust and power coefficients and the propulsive efficiency at altitude of 16 km for different blade structures at 1751 rpm

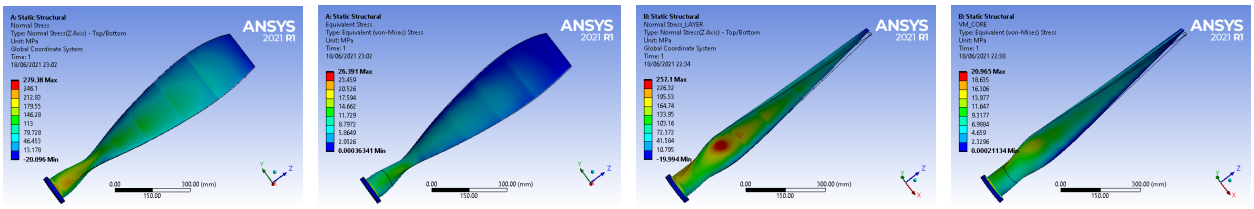

(a) Composite layer Normal stress by centrifugal force only.

(b) 3D printed core VM stress by centrifugal force only.

(c) Composite layer Normal stress by FSI at H=0 km.

(d) 3D printed core VM stress by FSI at H=0 km.

Fig. 14 3D printed tough PLA blade stress distribution.

and 1962 rpm as shown in Fig .15.

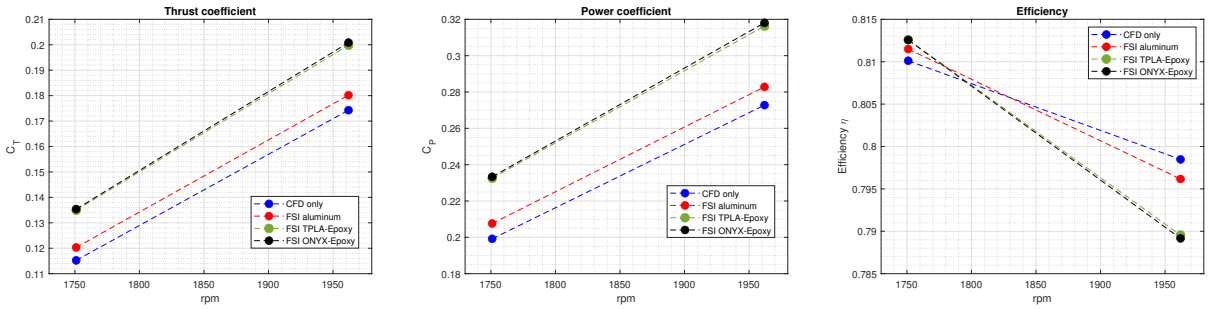

(a) Thrust coefficient.

(b) Power coefficient.

(c) Efficiency.

Fig. 15 Performance comparison between rigid and deformed propeller blades at altitude of 16 km.

It can be seen, from Fig .15a and Fig .15b, that the thrust and the torque generated by the deformed blade (FSI) are greater than those generated by the rigid one (CFD) for all the materials because of the twisting moment and the resulting increase in angle of attack. The aluminum blade shows an increase of 4.4% and 3.4% in thrust with an increase of 4.2% and 3.7% in torque for 1751 rpm and 1962 rpm respectively, resulting in a slight improvement in terms of efficiency for 1751 rpm (+0.14%) and a small loss for 1962 rpm (−0.23%) as shown in Fig .15c. Both the 3D printed blades (TPLA and Onyx) show almost the same performance due to the composite layer covering the blade surface, which supports the majority of the loads and imposes the same deformation for the two 3D printed cores. In this case, the thrust increases by 17.5% and 15.2% with an increase of 17.1% and 16.6% in torque for 1751 rpm and 1962 rpm respectively, resulting in better improvement in terms of efficiency for 1751 rpm (+0.24%) and a loss for 1962 rpm (−0.9%). These differences show that even for blades made of rigid materials, FSI calculations are paramount for an accurate prediction of the efficiency.

Fig .16 and Fig .17 show the difference in pressure and skin friction distribution between the rigid and the deformed blades at two cross-sections (70% and 90% of the blade radius). The pressure coefficient C_p and the skin friction coefficient C_f are presented for different blade structures in the same graph for each operating point and each cross-section. The dynamic pressure used to calculate these coefficients is defined as: $q_\infty = 0.5\rho(V_\infty^2 + (2\pi nr)^2)$.

In both radial positions and both operating points, the pressure load is increased when comparing to the CFD-only case especially in the first half of the airfoil chord length (leading edge side). This is accompanied by a higher skin friction coefficient in the same region. This explains the gain in thrust and the increase of torque while keeping almost the same propulsive efficiency (less than ±1%). The difference in C_p and C_f is due to the increase of the blade pitch angle after deformation, and the amount of the deformation depends on the material characteristics. The aluminum is stiffer and more rigid than the 3D printed materials, which gives less deformation and a deformed shape closer to the design shape, but it is heavier and denser especially in the case of a large scale propeller.

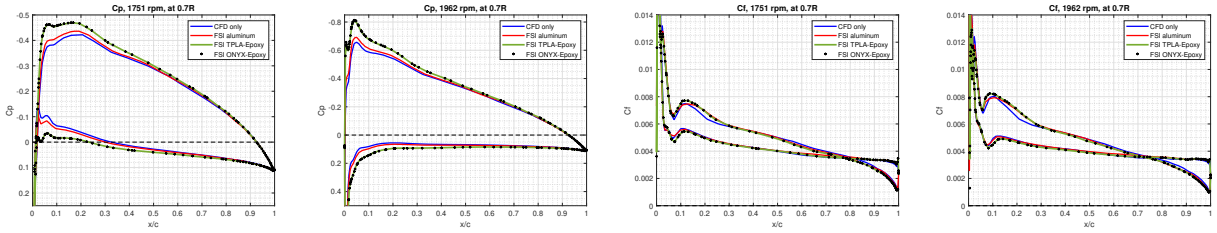

(a) 1751 rpm. (b) 1962 rpm. (c) 1751 rpm. (d) 1962 rpm.

Fig. 16 Pressure coefficient (a) and (b) and skin friction coefficient (c) and (d) at 0.7R.

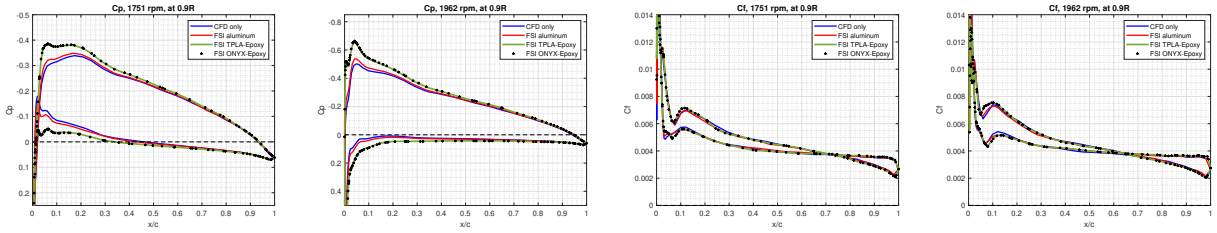

(a) 1751 rpm. (b) 1962 rpm. (c) 1751 rpm. (d) 1962 rpm.

Fig. 17 Pressure coefficient (a) and (b) and skin friction coefficient (c) and (d) at 0.9R.

V. Conclusion

In this study, a steady aeroelastic fluid-structure interaction analysis of a high altitude propeller blade has been carried out. The blade radius is 0.95 m and its geometry is obtained from an optimization process based on low fidelity models. ANSYS Fluent and ANSYS Mechanical have been coupled through ANSYS System Coupling to enable the force and displacement transfer between the fluid and the solid solvers. The blade structure is based on thermoplastic 3D printing materials. Two thermoplastic materials are used in this study: tough PLA printed by Ultimaker S5 printer characterized by a linear stress-strain relation, and Onyx printed by Markforged which has a nonlinear behaviour, in addition to an aluminum blade as benchmark. Tough PLA is modeled using the linear elastic model, whereas Onyx is modeled using the hyper-elastic experimental data toolbox in ANSYS. The two 3D printed blades are covered by a composite layer consisting of Epoxy S-glass UD to improve their strength and obtain a smooth external surface.

The steady aeroelastic results show that the blade angle is increased due to the blade deformation, resulting in a gain of thrust between 3.4% and 4.4% for the aluminum blade accompanied with an increase of 3.7% and 4.2% in torque, whereas the 3D printed blades have a gain of 15.2% to 17.5% with an increase of 16.6% and 17.1% in torque. The quasi-proportional increase in the aerodynamic forces keeps the same range of propulsive efficiency with slight variations (less than $\pm 1\%$). The study also shows that the centrifugal forces are dominant at high altitude in terms of stress and deformation due to the relatively low values of the aerodynamic forces. At sea level, the air is denser and the aerodynamic forces are more important and they are dominant in terms of deformation but the centrifugal forces are still dominant in terms of stress. In addition, the majority of the blade loads are supported by the composite layer which imposes almost the same deformation to the 3D printed blades, resulting in similar aerodynamic performance. Since the positive or negative effect of deformation on the propulsive efficiency depends on the operating conditions as well as the blade structure and materials, FSI analyses should be used in future propeller blade studies.

In future work, the blade weight could be reduced by creating internal holes in the 3D printed cores, thus the centrifugal force is reduced leading to a compromise with the stress level in the blade cores since the blade section area is reduced as well. Structural optimization could also be conducted with as objective the weight reduction which is directly related to the printing time reduction and the 3D printed material consumption.

Acknowledgments

The authors would like to acknowledge The Royal Higher Institude for Defense for funding this research through project MSP19/08 Tailored High Altitude Propeller in collaboration with Stratos Solutions.

The authors acknowledge J. Paesmans and B. J. Vansprengel master interns from Vrije Universiteit Brussel at the Royal Military Academy for their contribution for this study.

References

[1] Gonzalo, J., López, D., Domínguez, D., García, A., and Escapa, A., "On the capabilities and limitations of high altitude pseudo-satellites," *Progress in Aerospace Sciences*, Vol. 98, 2018, pp. 37–56. https://doi.org/10.1016/j.paerosci.2018.03.006.

[2] Marinus, B. G., Mourousias, N., and Malim, A., "Exploratory Optimizations of Propeller Blades for a High-Altitude Pseudo-Satellite," *AIAA Aviation 2020 Forum*, 2020, p. 2798. https://doi.org/10.2514/6.2020-2798.

[3] Weick, F. E., *Aircraft propeller design*, McGraw-Hill Book Company, inc, New York, 1930.

[4] Ammat, W., Bates, W. E., and Borst, H. V., "Summary of propeller design procedures and data Volume II–Structural analysis and blade design," *U.S. Army Air Mobility Research and Development Laboratory Technical Report*, Nov. 1973.

[5] Marinus, B., "Multidisciplinary optimization of aircraft propeller blades," Ph.D. thesis, Ecully, Ecole centrale de Lyon, 2011.

[6] Toleos Jr, L. R., Luna, N. J. A. B. D., Manuel, M. C. E., Chua, J. M. R., Sangalang, E. M. A., and So, P. C., "Feasibility Study for Fused Deposition Modeling (FDM) 3D-Printed Propellers for Unmanned Aerial Vehicles," *International Journal of Mechanical Engineering and Robotics Research*, Vol. 9, No. 4, April 2020, pp. 548–558. https://doi.org/10.18178/ijmerr.9.4.548-558.

[7] Khaleed, H., Badruddin, I. A., Saquib, A., Addas, M., Kamangar, S., and Khan, Y., "Novel Approach to Manufacture an AUV Propeller by Additive Manufacturing and Error Analysis," *Applied Sciences*, Vol. 9, No. 20, 2019, p. 4413. https://doi.org/10.3390/app9204413.

[8] Biswas, P., Heryudono, A., Li, J., and Bi, J., "Prediction of Printing Failure of a 3D Printed Drone Propeller using Fused Deposition Modeling," 2018.

[9] Rutkay, B. D., "A process for the design and manufacture of propellers for small unmanned aerial vehicles," Ph.D. thesis, Carleton University, 2014.

[10] Turner, B. N., Strong, R., and Gold, S. A., "A review of melt extrusion additive manufacturing processes: I. Process design and modeling," *Rapid Prototyping Journal*, Vol. 20, No. 3, 2014, pp. 192–204. https://doi.org/10.1108/RPJ-01-2013-0012.

[11] Turner, B. N., and Gold, S. A., "A review of melt extrusion additive manufacturing processes: II. Materials, dimensional accuracy, and surface roughness," *Rapid Prototyping Journal*, Vol. 21, No. 3, 2015, pp. 250–261. https://doi.org/10.1108/RPJ-02-2013-0017.

[12] Kumar, L. J., and Nair, C. K., "Current trends of additive manufacturing in the aerospace industry," *Advances in 3D printing & additive manufacturing technologies*, Springer, 2017, pp. 39–54. https://doi.org/10.1007/978-981-10-0812-2_4.

[13] Zadpoor, A. A., and Malda, J., "Additive manufacturing of biomaterials, tissues, and organs," *Annals of Biomedical Engineering*, Vol. 45, No. 1, 2017, pp. 1–11. https://doi.org/10.1007/s10439-016-1719-y.

[14] Lee, J.-Y., An, J., and Chua, C. K., "Fundamentals and applications of 3D printing for novel materials," *Applied Materials Today*, Vol. 7, 2017, pp. 120–133. https://doi.org/10.1016/j.apmt.2017.02.004.

[15] Shahrubudin, N., Lee, T., and Ramlan, R., "An overview on 3D printing technology: technological, materials, and applications," *Procedia Manufacturing*, Vol. 35, 2019, pp. 1286–1296. https://doi.org/10.1016/j.promfg.2019.06.089.

[16] Qu, Z., and Yang, Y., "Aeroelastic Analysis for the High Altitude Propeller by Using Fluid-Structure Interaction Method," *Transactions of the Japan Society for Aeronautical and Space Sciences, Aerospace Technology Japan*, Vol. 16, No. 3, 2018, pp. 236–241.

[17] Carnie, G., and Qin, N., "Fluid-structure interaction of HALE wing configuration with an efficient moving grid method," *46th AIAA Aerospace Sciences Meeting and Exhibit*, 2008, p. 309.

[18] Sodja, J., De Breuker, R., Nozak, D., Drazumeric, R., and Marzocca, P., "High-and Low-Fidelity Investigations of Flexible Propeller Blades," *52nd Aerospace Sciences Meeting*, 2014, p. 0410.

[19] Sodja, J., De Breuker, R., Nozak, D., Drazumeric, R., and Marzocca, P., "Assessment of low-fidelity fluid–structure interaction model for flexible propeller blades," *Aerospace Science and Technology*, Vol. 78, 2018, pp. 71–88.

[20] Reynolds, R. M., Sammonds, R. I., and Walker, J. H., *An Investigation of Single-and Dual-rotation Propellers at Positive and Negative Thrust, and in Combination with an NACA 1-series D-type Cowling at Mach Numbers Up to 0.84*, Technical Report TR-1336, NACA, NACA-Ames aeronautical laboratory (USA), 1957.

[21] Fahrenholz, H., "The 2012 version of ISO 527 plastics: determination of tensile properties," *Zwick/Roell*, 2018.